JACS
JOURNAL OF THE AMERICAN CHEMICAL SOCIETY
pubs.acs.org/JACS
Article

Electron Redistribution within the Nitrogenase Active Site FeMo-Cofactor During Reductive Elimination of H_2 to Achieve N≡N Triple-Bond Activation

Dmitriy A. Lukoyanov, Zhi-Yong Yang, Dennis R. Dean, Lance C. Seefeldt, Simone Raugei, and Brian M. Hoffman*

Cite This: J. Am. Chem. Soc. 2020, 142, 21679–21690
Read Online

ABSTRACT: Nitrogen fixation by nitrogenase begins with the accumulation of four reducing equivalents at the active-site FeMo-cofactor (FeMo-co), generating a state (denoted $E_4(4H)$) with two [Fe−H−Fe] bridging hydrides. Recently, photolytic reductive elimination (*re*) of the $E_4(4H)$ hydrides showed that enzymatic *re* of $E_4(4H)$ hydride yields an H_2-bound complex ($E_4(H_2,2H)$), in a process corresponding to a formal 2-electron reduction of the metal-ion core of FeMo-co. The resulting electron-density redistribution from Fe−H bonds to the metal ions themselves enables N_2 to bind with concomitant H_2 release, a process illuminated here by QM/MM molecular dynamics simulations. What is the nature of this redistribution? Although $E_4(H_2,2H)$ has not been trapped, cryogenic photolysis of $E_4(4H)$ provides a means to address this question. Photolysis of $E_4(4H)$ causes hydride-*re* with release of H_2, generating doubly reduced FeMo-co (denoted $E_4(2H)^*$), the extreme limit of the electron-density redistribution upon formation of $E_4(H_2,2H)$. Here we examine the doubly reduced FeMo-co core of the $E_4(2H)^*$ limiting-state by ^1H, ^{57}Fe, and ^{95}Mo ENDOR to illuminate the partial electron-density redistribution upon $E_4(H_2,2H)$ formation during catalysis, complementing these results with corresponding DFT computations. Inferences from the $E_4(2H)^*$ ENDOR results as extended by DFT computations include (i) the Mo-site participates negligibly, and overall it is unlikely that Mo changes valency throughout the catalytic cycle; and (ii) two distinctive $E_4(4H)$ ^{57}Fe signals are suggested as associated with structurally identified "anchors" of one bridging hydride, two others with identified anchors of the second, with NBO-analysis further identifying one anchor of each hydride as a major recipient of electrons released upon breaking Fe−H bonds.

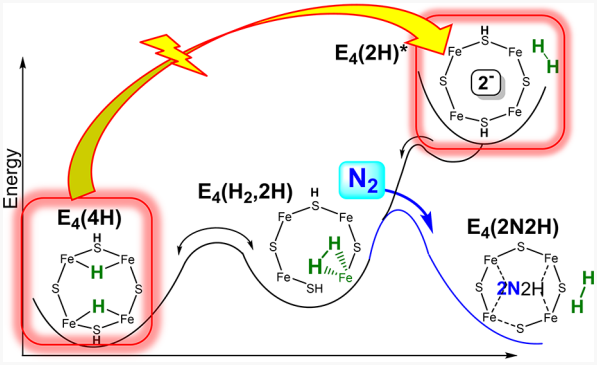

INTRODUCTION

Nitrogen fixation by nitrogenase, the reduction of N_2 to two NH_3, is initiated by the accumulation of four reducing equivalents at the active site FeMo-cofactor (FeMo-co).[1] We have demonstrated that this generates a state (denoted $E_4(4H)$, the Janus intermediate) with two [Fe−H−Fe] bridging hydrides, two sulfur-bound protons, and a metal-ion core that is formally at the resting-state redox-level.[2−4] This state is activated for the highly endergonic N_2 binding/cleavage of the N≡N triple bond by the mechanistically coupled reductive elimination (*re*) of the hydrides and exergonic release of H_2. This process and its reverse, the oxidative addition (*oa*) of H_2 by $E_4(2N2H)$ with release of N_2, together form an approximately isoenergetic *re*/*oa* equilibrium, Figure 1, which is central to nitrogenase catalysis and whose operation implies the limiting stoichiometry of eight electrons/protons for the reduction of N_2 to two NH_3 (eq 1).[2−4]

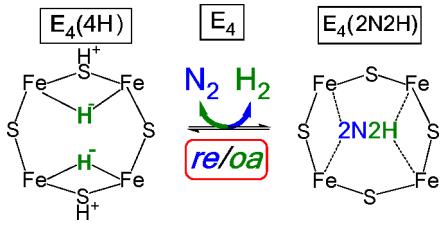

Figure 1. Representation of the *re*/*oa* equilibrium that activates nitrogenase to break the N≡N triple bond. Cartoons represent the Fe 2,3,6,7 face of FeMo-co, with $E_4(4H)$ representing the actual structure and $E_4(2N2H)$ merely representing the stoichiometry for the unknown structure.

Received: July 22, 2020
Published: December 16, 2020

https://dx.doi.org/10.1021/jacs.0c07914
J. Am. Chem. Soc. 2020, 142, 21679−21690

$$N_2 + 8e^- + 16ATP + 8H^+ \rightarrow 2NH_3 + H_2 + 16ADP + 16P_i \quad (1)$$

As dihydride *re* and the release of H_2 are the key to nitrogen fixation, the details are of central importance. By exploiting the ability of the dihydride metal complex to undergo photolytic reductive elimination of H_2,[5] our photolytic studies of nitrogenase have shown[6−8] that during catalysis the *re* of hydrides converts $E_4(4H)$ to an H_2-bound complex, denoted $E_4(H_2,2H)$, on the ground (catalytic) adiabatic potential energy surface (PES) (Figure 2). The *re* of the two $E_4(4H)$

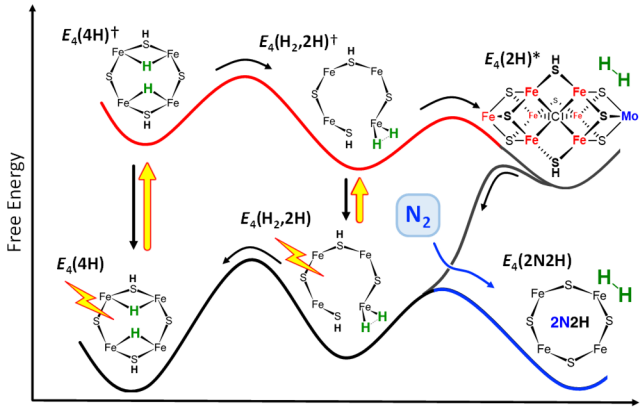

Figure 2. Schematic representation of ground (black and blue) and photoexcited (red) free energy surface for *re*/*oa* equilibrium, where (†) represents a photoexcited state and (*) the high-energy product of H_2 release on the ground surface (ref 9).

hydrides, which corresponds to a 2-electron reduction of the metal-ion core of $E_4(H_2,2H)$, which formally makes it doubly reduced relative to E_0, redistributes electron density from the metal-hydride bonds of $E_4(4H)$ to the metal ions themselves. This redistribution enables N_2 to bind and react with $E_4(H_2,2H)$ to form $E_4(2N2H)$ and release H_2.

One might imagine several alternatives for the process by which N_2 is bound and H_2 is lost during the conversion of $E_4(H_2,2H)$ to $E_4(2N2H)$. Early experiments[1] showed that this conversion does not occur by the following two discrete, successive steps: (i) loss of H_2, which carries away two of the accumulated electrons to form a high-energy state, denoted $E_4(2H)$*, in which the core is doubly reduced relative to the resting state; (ii) subsequent N_2 binding/reduction by this activated cofactor. In such a two-step mechanism, operation of the *re*/*oa* equilibrium would require that during turnover under D_2 in the absence of N_2, the D_2 would react with $E_4(2H)$* through *oa*, generating the E_4 state with two bridging deuterides that can relax with release of HD, but it has long been known that this does not occur.[1] Thus, during catalysis N_2 must concertedly bind-to/react-with the H_2 complex, through a combination of N_2-cofactor bond-making and H_2-cofactor bond-breaking that leads to H_2 release and N_2 triple-bond cleavage (Figure 2). This picture is given in microscopic form through density functional theory (DFT) computations, which show why H_2 cannot simply be released from $E_4(H_2,2H)$ to form a doubly reduced FeMo-co, $E_4(2H)$*, the high-energy product of H_2 reductive elimination (Figure 2): it is not energetically feasible.[9] The shift of electron density from the Fe−H−Fe linkages to the metal-ion core upon formation of $E_4(H_2,2H)$ must instead be sufficient to enable N_2 binding to form a transient state with both H_2 and N_2 bound (denoted here as $E_4(H_2,N_2,2H)$), which releases H_2 to form $E_4(2N2H)$. More recent computations by Bjornsson and co-workers identified $E_4(H_2,2H)$ as the lowest-energy E_4 isomer but suggested that N_2 binds to an higher energy E_4 isomer having two geminal bridging hydrides, which after N_2 coordination releases H_2 by *re*.[10]

What is the nature of the increase in electron density on the FeMo-co core when the two hydrides of $E_4(4H)$ are reductively eliminated to form the bound H_2 of $E_4(H_2,2H)$? Although $E_4(H_2,2H)$ itself has not yet been trapped for study, the photolysis of $E_4(4H)$ has given us a means to address this question. Photolysis of $E_4(4H)$ at cryogenic temperatures causes the reductive elimination and release of H_2 to form an excited H_2 complex on the excited potential energy surface (PES) which goes on to release the H_2 and relax to the high-energy $E_4(2H)$* state on the catalytic (ground) PES (Figure 2). The high-energy $S = 1/2$ $E_4(2H)$* state achieves a full 2-electron reduction of the FeMo-co core relative to the resting state (Scheme 1).[6−8] The $S = 1/2$ $E_4(2H)$* state, with its

Scheme 1

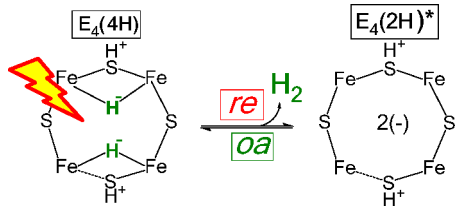

doubly reduced core and two protons on sulfides, is formed in a cryogenically frozen matrix and therefore is unable to relax to the "isomeric" $S = 3/2$, $E_2(2H)$ state generated by two sequential steps of $[e^-/H^+]$ delivery during turnover. Whereas $E_2(2H)$ is relatively unreactive because the two electrons are "stabilized" by forming a bridging [Fe−H−Fe] hydride (one proton is bound to sulfide), the $E_4(2H)$* state represents the extreme form of reductive activation of the FeMo-co core that occurs through the increase in and redistribution of electron density that occurs upon formation of $E_4(H_2,2H)$ on the catalytic PES (Figure 2).

We have examined the doubly reduced FeMo-co core of the $E_4(2H)$* limiting state to shed light on the partial electron density redistribution during catalysis. In this report, we describe ^{1}H, ^{57}Fe, and ^{95}Mo electron-nuclear double resonance spectroscopy (ENDOR) of $E_4(2H)$* and compare these properties to those of the FeMo-co core of the Janus intermediate precursor, $E_4(4H)$, which is formally at the resting state valency, and to the E_0 resting state itself. We complement these results with corresponding DFT comparisons of these states, which associate two ^{57}Fe $E_4(4H)$ ENDOR signals with structurally identified "anchors" of one bridging hydride, two others with anchors of the second, while identifying one anchor of each hydride as a major recipient of electrons released upon breaking Fe−H bonds.

MATERIALS AND METHODS

Preparation of Turnover Samples for EPR and ENDOR Measurements. The samples of V70I $E_4(4H)$ employed here were described previously: natural abundance and ^{95}Mo-enriched[11] and ^{57}Fe-enriched.[12] The $E_4(2H)$* state was generated for X/Q-band electron paramagnetic resonance (EPR) and Q-band ENDOR spectroscopy examination by 450 nm illumination of a Q-band tube

https://dx.doi.org/10.1021/jacs.0c07914
J. Am. Chem. Soc. 2020, 142, 21679−21690

of the corresponding $E_4(4H)$ intermediate for about 1 h in the X-band EPR cavity at 12 K,[6−8] which caused ∼80% conversion. The photolyzed samples were stored for characterization in liquid nitrogen, where the $E_4(2H)$* state is stable indefinitely.

EPR and ENDOR Measurements. Continuous wave (CW) X-band EPR spectra were collected on a Bruker ESP 300 spectrometer equipped with a continuous helium flow cryostat Oxford Instruments ESR 900. The CW 35 GHz EPR and ENDOR spectra were obtained on a modified Varian E-110 spectrometer equipped with a helium immersion Dewar at 2 K under "rapid passage" conditions using 100 kHz magnetic field modulation.[13] Pulsed 35 GHz ENDOR spectra were recorded at 2 K on a locally constructed spectrometer.[14]

^{1}H and ^{57}Fe nuclei have nuclear spin $I = 1/2$, and the ENDOR spectrum from a single orientation of the paramagnetic center relative to the external field is a doublet centered at the nuclear Larmor frequency, ν_N and split by the orientation-dependent hyperfine coupling, A. ^{95}Mo has a nuclear spin, $I = 5/2$, and for ^{95}Mo ENDOR spectra in principle, a single orientation can exhibit a pattern of $2I = 10$ lines whose frequencies depend on the nuclear Larmor frequency, hyperfine coupling, and nuclear quadrupole coupling. However, ^{95}Mo ENDOR spectra of nitrogenase are dominated by a doublet associated with the nuclear spin projection values, $m_I = \pm 1/2$ centered at the nuclear Larmor frequency, ν_{Mo} and split by the orientation-dependent hyperfine coupling, A; the other, "satellite" transitions are absent in most spectra and when present are seen only as unresolved ENDOR intensity; these features are attributable to a large quadrupole coupling with distributed values of the tensor components/orientation.[44,45] The properties of the orientation-dependent hyperfine coupling tensor were estimated by examining a 2D field-frequency pattern of ENDOR spectra taken across the EPR spectrum.

Signs of the hyperfine couplings (more specifically, the sign of $g_{Nuc}A_{Nuc}$) were obtained by the PESTRE protocol,[15] a pulsed-ENDOR multisequence comprising multiple Davies ENDOR sequences, carried out in three distinct experimental phases: (I) an EPR saturation phase (RF off) in which spin−echo intensities quickly converge to the steady-state "baseline" (BSL); (II) sequences that contain a fixed RF frequency; and (III) an EPR recovery phase (RF off) during which the spin echo intensity, the "dynamic reference level (DRL)", relaxes to BSL. The sign of A_{Nuc} is unambiguously given by the sign of the decaying difference in echo intensities, (DRL − BSL), as observed in III. When $A_{Nuc} > 0$ (and $g_{Nuc} > 0$), if ν_+/ν_- is being interrogated, the DRL relaxes to the BSL from below/above. When $A_{Nuc} < 0$, the opposite behavior is observed.

Computational Details. *Hybrid QM/MM Metadynamics Simulations.* The thermal reorganization of hydrogen atoms in the E_4 state was investigated via *ab initio* QM/MM Born−Oppenheimer metadynamics molecular dynamics simulations.[16−22] The FeMo-co, its environment, and the four accumulated hydrogens were treated at the QM level, whereas the rest of the nitrogenase complex, solvent, and counterions were described according to the amber force field.[23] As discussed in detail elsewhere,[9] the QM region comprises the FeMo-co with truncated modifications of the α-275^{Cys}, α-442^{His} ligands (*Azotobacter vinelandii* numbering), R-homocitrate, and all of the MoFe protein residues and water molecules that are either hydrogen-bonded to the FeMo-co as obtained from molecular dynamics simulations or are known to be important of the catalytic activity (α-70^{Val} and α-96^{Arg}). The parts of the protein that interact with FeMo-co via hydrogen bonds residues are α-278^{Ser} (interacting with the S atom of α-275^{Cys}), α-195^{His} (interacting with S2B atom of FeMo-co), and the backbone of α-356^{Gly}, α-357^{Gly}, 358^{Leu}, and α-359^{Arg} (which interacts with S3A). The side chain of α-359^{Arg}, which is adjacent to the Fe_3−Fe_7 side, was also included. Additionally, water molecules (three molecules) present in the pocket next to the Fe_3−Fe_7 side and a molecule bridging the homocitrate and S5A were explicitly treated at the QM level. Residues α-278^{Ser}, α-275^{Cys}, α-195^{His} were truncated at the Cα−Cβ bond; α-96^{Arg} was truncated at the Cδ−Cγ bond; α-359^{Arg} was included in its entirety; only the backbone α-356^{Gly}, α-357^{Gly}, 358^{Leu} was included; finally homocitrate was truncated at the C_1−C_2 and C_4−C_5 bonds. The adopted QM model contains 148 atoms, and it is illustrated in Figure S3. The generalized hybrid orbital method for the treatment of the QM/MM boundary atoms was adopted.[24]

The Amber FF14SB force field was adopted to describe the protein[25] along with the TIP3P model for water molecules,[26] whereas the force field parameters for the P cluster, FeMo-co, and cubane were taken from our previous work.[27] The QM calculations were performed in the broken symmetry (BS)-density functional theory (DFT) framework with the BP86 exchange and correlation functional, augmented with Grimme's correction for the dispersion energy (BP86+D3).[28−31] The Kohn−Sham wave functions of the valence electrons were expanded with a triple-ζ Gaussian basis set with added polarization functions and an auxiliary plane wave basis set with a 400 Ry cutoff. Core electrons were described with Goedecker−Teter−Hutter pseudopotentials.[32,33]

The QM/MM simulations where started from an equilibrated snapshot obtained from force-field-only molecular dynamics simulations and using the lowest energy BP86 BS solution as found in ref 9 (Fe_1↓, Fe_2↑, Fe_3↑, Fe_4↑, Fe_5↓, Fe_6↑, Fe_7↓, Mo↓, where the arrows indicates spin up or down). The QM/MM system was equilibrated at 298 K for 15 ps using a Nosé−Hoover chain of thermostats.[34] To reconstruct the free energy landscape for the hydrogen exchange at room temperature, an adaptive biasing force technique based on a coarse-grained history-dependent dynamics (metadynamics) was employed (see the Supporting Information for more details).[16,17] The coordination numbers of the pairs Fe_2/Fe_6 and Fe_3/Fe_7 to the hydrogen atoms were employed to study the hydrogen movement between the Fe_2/Fe_6 and Fe_3/Fe_7 sides of the reactive face of the FeMo-co. A (continuous) coordination coordinate based on the Fe−H distances was introduced for each pair of Fe atoms, which assumes the ideal values 0, 1, and 2, if no, one, or two hydrogens are coordinated to a given pair.[16] As discussed in the Supporting Information and defined there in eq S1, the coordination number can assume values that deviate appreciably from the ideal values listed above. This is a feature that allows discriminating between various E_4 isomers. For instance it is larger than 2 if two hydrogen atoms are equally shared between two Fe atoms as is the case for the geminal bridging dihydride $E_4(4H)^{(c)}$ (see the Supporting Information for further information). Gaussian functions of 0.4 kJ/mol height and 0.05 width were added every 50 fs to bias the coordination number space. The metadynamics simulations were started from an equilibrated QM/MM configuration of the $E_4(4H)^{(a)}$ isomer and interrupted when the system returned to the $E_4(4H)^{(a)}$ state (after about 32 ps). All QM/MM simulations were performed with a time step of 0.25 fs using the CP2K package.[18] The QM/MM trajectories will be made available upon request.

Natural Bond Orbital Analysis of the Electron Density. The electron distribution for the various E_4 isomers was analyzed with the natural bond orbital (NBO) theory using truncated QM models;[35] for further discussion of the NBO analysis, see the Supporting Information. The QM models are as in the QM/MM simulation above. The Ahlrichs VTZ basis set was used for all Fe atoms; the LANL2TZ basis set with an effective core potential was employed for the Mo atom, and the 6-311++G** basis set was employed for all atoms coordinated to metal atoms and finally the 6-31G* basis set was adopted for all other atoms.[36−38] All QM calculations were performed with the NWChem quantum chemistry package and the NBO analysis carried out with NBO6.0 software.[39,40]

RESULTS

EPR. The $S = 1/2$ $E_4(4H)$ produced by Ar turnover was subject to prolonged irradiation with light of 450 nm at cryogenic temperatures, which converts $E_4(4H)$, g = [2.150, 2.007, 1.965], almost completely into $S = 1/2$ $E_4(2H)$*, g = [2.098, 2.000, 1.956] (Figure 3). Additional intensity to higher field than these two signals is associated with the electron-delivery reduced Fe protein. We earlier showed that $E_4(4H)$ is the ground state, with no low-lying states becoming populated

https://dx.doi.org/10.1021/jacs.0c07914
J. Am. Chem. Soc. 2020, 142, 21679−21690

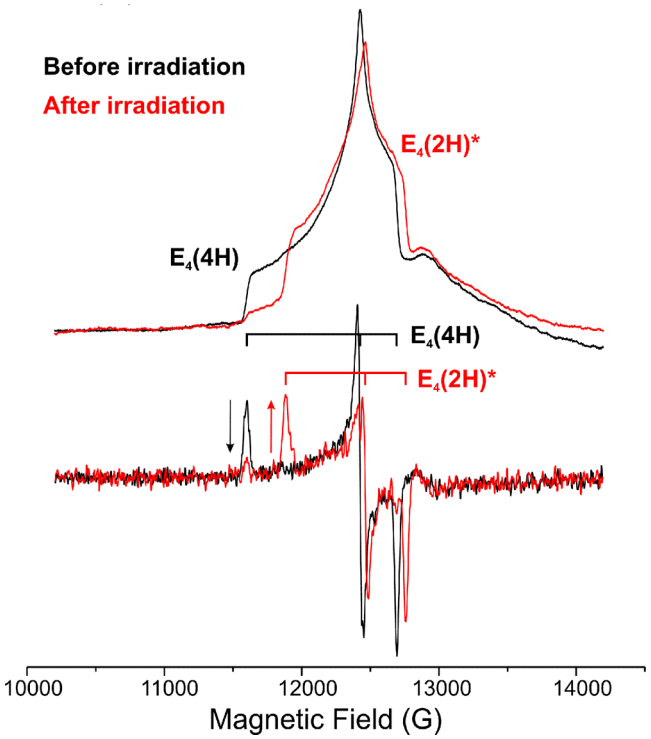

Figure 3. Q-band CW EPR spectra of ^{57}Fe enriched V70I nitrogenase trapped during turnover under Ar taken at 2 K before (black) and after (red) irradiation with 450 nm laser diode at 12 K. The spectra were obtained in dispersion mode under rapid passage conditions, which yields the upper absorption-display spectra; the lower traces are digital derivatives. EPR conditions: microwave frequency, 35.08 GHz; microwave power, 10 μW; modulation amplitude, 1 G; time constant, 128 ms; scan time, 4 min.

before the signal broadens and disappears at ~25 K,[12] and the same is true for $E_4(2H)$*.

^{1}H Couplings in $E_4(2H)$*. We recall here that the large, rhombic ^{1}H hyperfine couplings to the two [Fe−H−Fe] of $E_4(4H)$ seen as splittings in its EPR spectrum (Figure S1) and fully characterized by ENDOR spectroscopy[41] are absent in $E_4(2H)$*, observations which defined $E_4(2H)$* as the product of photoinduced *re* of the hydrides and loss of H_2.[7,8] Examination of the remaining ^{1}H ENDOR responses of $E_4(2H)$* shows signals from bridging or terminal SH with couplings similar to those of $E_4(4H)$ (maximum couplings of 8−10 MHz).

^{95}Mo Hyperfine Coupling in $E_4(2H)$*. The Mo of resting-state E_0 cofactor has been identified as a non-Hund's-rule Mo(III),[42,43] but as explained below, it shows the small ^{95}Mo coupling measured in the earliest nitrogenase ENDOR studies: a_{iso} ~−6 MHz upon correcting the sign of the nuclear *g*-factor used previously to −0.3656.[44,45] The sign of the ^{95}Mo hyperfine coupling for the $S = 3/2$ E_0 was determined through analysis of the pseudonuclear Zeeman effect, which converts the intrinsic ^{95}Mo Larmor frequency $\nu(^{95}\text{Mo})^0$ into an experimentally observed larger effective frequency $\nu(^{95}\text{Mo})$ for negative hyperfine coupling;[46] this effect is not operative in the $S = 1/2$ $E_4(4H)$ and the negative sign for this state is assumed to be the same as for E_0 because they are formally at the same redox state. Later 35 GHz CW ENDOR measurements[47,44,45] revealed that the ^{95}Mo enriched $S = 1/2$ $E_4(4H)$ intermediate exhibits a very small and essentially isotropic ^{95}Mo hyperfine coupling, a_{iso} ~−4 MHz, Figure 4, not meaningfully different from the ^{95}Mo coupling of the WT E_0 state.

As the first probe of the ^{95}Mo hyperfine coupling in the two-electron reduced cofactor of $E_4(2H)$* and for a possible increase in the coupling because of valency and/or spin-coupling changes at Mo upon FeMo-co reduction, we looked for EPR line-broadening in ^{95}Mo enriched samples. Comparison between the EPR spectra of natural-abundance and ^{95}Mo-enriched $E_4(2H)$* shows no noticeable broadening upon the ^{95}Mo enrichment (Figure S1), demonstrating that there is no appreciable increase in the ^{95}Mo coupling in the two-electron reduced state $E_4(2H)$* (see the Supporting Information) and thus to a first approximation the coupling must remain roughly isotropic.

This conclusion was confirmed and the ^{95}Mo coupling of $E_4(2H)$* accurately determined by 35 GHz CW ENDOR measurements. Figure 4 compares the ENDOR spectra of ^{95}Mo-enriched $E_4(4H)$ formed during V70I Ar turnover with those taken after ≳70% photolytic conversion of $E_4(4H)$ to $E_4(2H)$*. The spectra of $E_4(4H)$ show the low-frequency ^{95}Mo signals reported previously.[47] The clearest comparison between the two states is provided by ENDOR measurements at fields corresponding to their g_3 values. In the EPR spectrum of $E_4(2H)$*, the g_3 feature does not overlap with that of residual $E_4(4H)$, whose value of g_3 is slightly larger (Figure 3), and thus the g_3 ENDOR spectra of the initial $E_4(4H)$ state and the photoinduced $E_4(2H)$* can be unambiguously compared.

A comparison of g_3 ENDOR spectra of natural-abundance and ^{95}Mo-enriched $E_4(2H)$* cleanly shows that enrichment introduces a ^{95}Mo doublet centered at the NMR frequency of ^{95}Mo and split by $A_3 = -2.7$ MHz (Figure 4, Figure S2), within error unchanged from that of $E_4(4H)$ (although the signal from the latter is broader) and unchanged from that of E_0 as well. Spectra taken across the EPR spectrum of $E_4(2H)$* show that the ^{95}Mo hyperfine coupling indeed remains essentially isotropic, Figure 4, Figure S2, and as inferred from the EPR spectra of Figure S1, with $|a_{iso}|$ ~3 MHz, little changed from that of $E_4(4H)$.

Our recent X-ray spectroscopic study of $E_1(H)$[48] showed that Mo retains the E_0 Mo(III) formal valence after the first stage of reduction, and our previous ^{95}Mo ENDOR study of $E_4(4H)$ suggested the same is true after four [e^-/H^+] additions to FeMo-co to generate $E_4(4H)$.[47] The equivalence of the ^{95}Mo couplings in $E_4(2H)$*, $E_4(4H)$, and E_0 extends this picture by indicating that the valence of Mo in the cofactors of $E_4(4H)$ and $E_4(2H)$* is the same as in resting state E_0. In particular, this invariance indicates that the valency and electronic structure of Mo in $E_4(2H)$* is not changed from that of $E_4(4H)$ by the photoinduced dihydride *re* and loss of H_2, with the attendant two-electron reduction of FeMo-co. This in turn indicates that the added electrons are distributed among the Fe ions, a conclusion that is consistent with the large changes in ^{57}Fe couplings described below. Although we thus infer that the Mo retains the E_0 Mo(III) formal valence in $E_4(2H)$* and in $E_4(4H)$,[47] the Mo in $E_4(2H)$* does sense the reduction, presumably through the influence of Mo−Fe bonding, as the small anisotropy in the ^{95}Mo coupling does change. The coupling for $E_4(4H)$ increases slightly at $g \sim g_2$ but decreases slightly for $E_4(2H)$*.

FeMo-co Spin Coupling and Metal-Ion Hyperfine Interactions. To analyze the metal-site ENDOR results for FeMo-co, we recall that the experimentally observed isotropic

https://dx.doi.org/10.1021/jacs.0c07914
J. Am. Chem. Soc. 2020, 142, 21679−21690

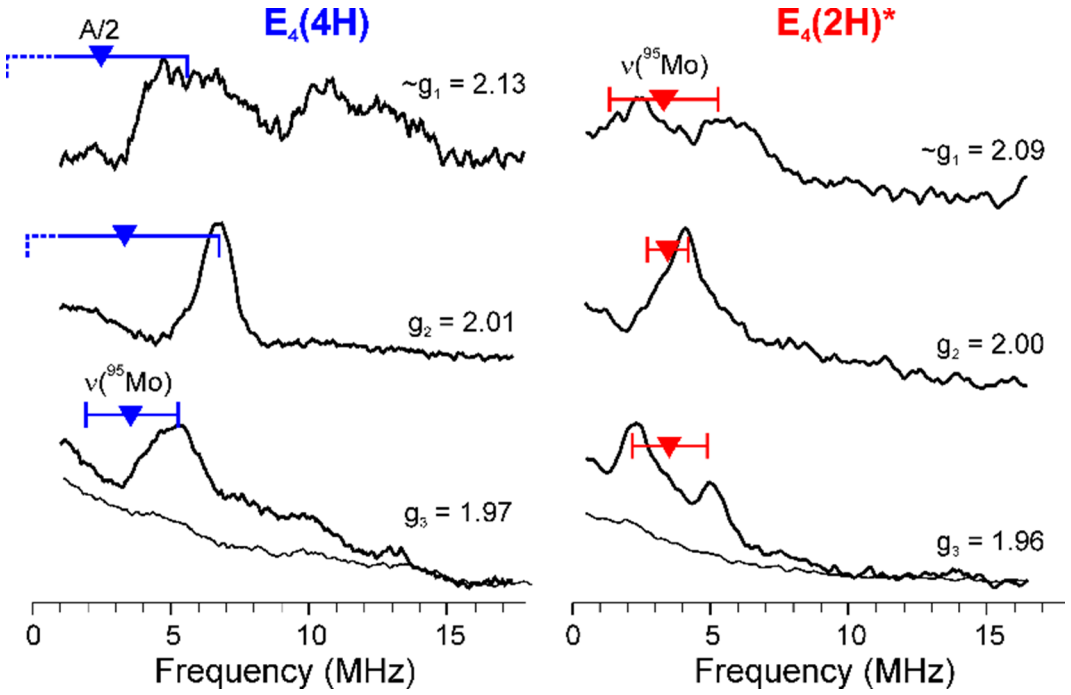

Figure 4. Comparison of ^{95}Mo CW ENDOR acquired at the three major g-values for E_4(4H) state trapped during Ar turnover of ^{95}Mo enriched V70I, as reported[47] and for E_4(2H)* photogenerated from E_4(4H) by irradiation with 450 nm laser diode at 12 K. "Goalposts" indicate ^{95}Mo (I = 5/2) transition between the $m_I = \pm 1/2$ nuclear sublevels with frequencies $\nu_\pm = |\nu(^{95}\text{Mo}) \pm A/2|$. Most of the spectra show the higher-frequency (ν_+) partner; the lower-frequency (ν_-) partner is at such a low frequency that it is not reliably detected. Spectra from unenriched enzyme are featureless, as demonstrate by the one included from g_3. Conditions: T = 2 K; microwave frequency, 35.1 and 34.8 GHz for E_4(4H) and E_4(2H)* correspondingly; microwave power, 1 μW and 0.1 μW; modulation amplitude, 4 and 1 G; RF sweep speed, 1 MHz/s and 2 MHz/s; time constant, 64 ms; RF bandwidth-broaden to 100 kHz.

hyperfine coupling to the ^{95}Mo, or to an ^{57}Fe nucleus of site i (see next subsection below) within the FeMo-co multinuclear spin-coupled cluster, a_i, is proportional to the intrinsic isotropic hyperfine coupling for the uncoupled metal ion site, a_i^{un}, multiplied by the projection of the total spin onto the local spin as a scaling factor, denoted K_i, with these projection factors subject to a normalization condition,

$$a_i = K_i a_i^{\text{un}}; \quad \sum_{i=1}^{n} K_i = 1 \tag{2}$$

where the summation is over n, the number of coupled metal ions.[49]

The Mo of resting-state cofactor recently has been identified as a non-Hund's-rule Mo(III),[42,43] and using the crudely estimated value $|a_{\text{iso}}(^{95}\text{Mo})^{\text{un}}| > 100$ MHz according to eq 2 the vector-coupling coefficient for Mo in each of these spin-coupled FeMo-co states must be very small, just as we concluded previously for E_0 (S = 3/2)[44,45] and E_4(4H) (S = 1/2).[47] Physically, a small vector-coupling coefficient K_{Mo} implies that the local Mo electron-spin is essentially orthogonal to the total cluster spin. For calculations with eq 2, a small K_{Mo} implies we may omit the contribution of the Mo site to the normalization sum over the K_i in this equation. This small coupling coefficient K_{Mo} of E_4(4H) was instrumental in the analysis that showed the two hydrides of this intermediate are not coordinated to Mo;[47] the symmetry of the hydride dipolar-interaction tensors identified the hydrides as bridging two iron ions, namely, are present as [Fe−H−Fe] moieties.[47,50,51]

Regarding the ^{57}Fe isotropic couplings, for second-row transition ions, and ^{57}Fe in particular the site (uncoupled) isotropic couplings are negative,[52] $a_i^{\text{un}} < 0$. Hence, according to eq 2, FeMo-co Fe sites with $a_i < 0$ have vector-coupling coefficients $K_i > 0$, while sites with positive coupling have $K_i < 0$.

^{57}Fe ENDOR. X-band EPR spectra of the ^{57}Fe-enriched V70I E_4(4H) and E_4(2H)* states, compared with spectra of the their natural abundance isotopomers (Figure S1) show the expected marked broadening induced by strong hyperfine interaction with multiple ^{57}Fe. CW ENDOR comparison of E_4(2H)* samples prepared with and without ^{57}Fe enrichment show the absence of any background signals in the low-frequency range of the ^{57}Fe signals (Figure S2). Complete 2D field-frequency plots of ^{57}Fe Q-band Davies ENDOR spectra were collected across the EPR envelope of E_4(4H) and the photolyzed E_4(2H)*-containing sample (Figure S3), with spectra collected at the canonical g-values shown in Figure 5. The amount of residual E_4(4H) state after illumination is so low that it can only noticeably contribute to the ^{57}Fe ENDOR spectra of the illuminated sample in a narrow range of fields near the maximum of the E_4(4H) EPR spectrum at g_2. Even in those spectra, residual signals were readily identified by reference to the ^{57}Fe ENDOR pattern of E_4(4H)[12] (Figure 5, Figure S3), thus enabling unambiguous identification and characterization of the E_4(2H)* ^{57}Fe responses in ENDOR spectra collected across the EPR envelope.

Comparison of the 35 GHz Davies pulsed ENDOR spectra taken at the three canonical g-values of the E_4(4H) and E_4(2H)* states reveals significant changes in the ^{57}Fe ENDOR spectra upon the conversion to E_4(2H)* (Figure 5). The most distinctive change is the absence of ^{57}Fe signals above 18 MHz for E_4(2H)*, as is most dramatically seen in the corresponding low-field, g_1 spectra. Whereas one of the ^{57}Fe of E_4(4H),

https://dx.doi.org/10.1021/jacs.0c07914
J. Am. Chem. Soc. 2020, 142, 21679−21690

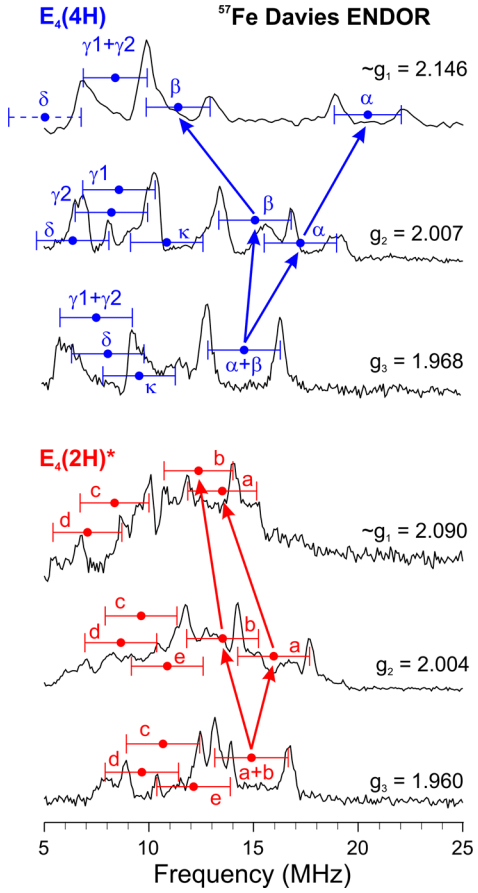

Figure 5. Comparison of ^{57}Fe Davies ENDOR acquired at three major g-values for E_4(4H) state trapped during Ar turnover of ^{57}Fe enriched V70I[12] and for E_4(2H)* photogenerated from E_4(4H) by irradiation with 450 nm laser diode at 12 K. "Goalposts" indicate response from one iron centered at half of its hyperfine coupling and split by $2\nu(^{57}\text{Fe})$. Conditions: T = 2 K; microwave frequency, 34.81 and 34.90 GHz for E_4(4H) and E_4(2H)* correspondingly; $t(\pi/2)$ = 40 ns, τ = 600 ns; T_{RF} = 35 μs; repetition time, 100 and 25 ms; 200–400 scans.

designated as α, exhibits an ENDOR doublet centered at ~20 MHz at g_1 which corresponds to a hyperfine coupling of ~40 MHz, the largest coupling for the E_4(2H)* at g_1 is associated with an ^{57}Fe doublet centered at ~13–14 MHz, corresponding to A ~ 27 MHz. Looking more broadly at the 2D patterns in Figure 5, Figure S3, for both centers the doublet with the largest coupling at the high-field, g_3 edge of the EPR spectrum is the overlap of doublets from two sites, and the hyperfine coupling to those two sites is about the same: A = 29 MHz for E_4(4H), A = 30 MHz for E_4(2H)*. However, these sites have very different hyperfine anisotropy in the two states. For E_4(4H), the couplings of the two sites still differ slightly at g_2, but at g_1 the coupling to one (α) has sharply increased to the strong coupling just discussed, A ~ 40 MHz, while the coupling to the other (β) has sharply decreased to A ~ 23 MHz. In contrast, for E_4(2H)*, these two sites show similar couplings across the EPR envelope, which decrease minimally at g_1, to A ~ 26 MHz.

The spectra of E_4(2H)* show increased "congestion" compared to those of E_4(4H) not only at the two single-crystal-like orientations g_1 and g_3 (Figure 5) but throughout the 2D pattern of spectra (Figure S3), because the hyperfine couplings of the ^{57}Fe sites of E_4(2H)* are more similar in magnitude and show smaller anisotropy. However, one can assign resolved signals throughout the 2D pattern to four of the seven irons of its cofactor and through much of the pattern to a fifth, denoted sites a–e (Figure 5). The ^{57}Fe ENDOR doublets for sites c, d, and e, observed in the lower frequency range at g_3, exhibit anisotropy broadening with increasing g-value (decreasing magnetic field), but like the sites a and b, the c, d, and e sites also do not exhibit strong anisotropy in their hyperfine interaction. The isotropic couplings derived from the 2D pattern for these five sites are listed in Table 1, with signs determined as described in the next paragraph. The values of a_{iso} for E_4(4H) and E_0 determined previously also are listed in the table.

Table 1. Isotropic ^{57}Fe Hyperfine Couplings[a]

E_4(2H)*[b]		E_4(4H)[c]		E_0[d]	
^{57}Fe	$a_{iso}/\delta A$[e] (MHz/%)	^{57}Fe	$a_{iso}/\delta A$[e] (MHz/%)	^{57}Fe	$a_{iso}/\delta A$[e] (MHz/%)
a	−30/+17	α	−35/−34	A^1	−18/+41
b	−27/+18	β	−27/+26	A^2	−17.1/23
e	+23	κ	~+20[g]	A^3	−11.8
f	~+25[f]	$\gamma 1$	+17	B^1	+11.7
g	~+25[f]	$\gamma 2$	−16	B^1	+11.7
c	−19	δ	+13	B^2	+9.3
d	−17	λ	~+8[g]	A^4	−3.7

[a]Isotropic hyperfine couplings (a_{iso}) of ^{57}Fe sites of photoreduced E_4(2H)*, Janus intermediate E_4(4H), and resting state E_0, arranged in order of absolute values; it is argued in the text that a/b, α/β, and A^1/A^2 refer to the same pair of Fe sites. [b]Isotropic coupling reported as average of coupling observed at canonical g-values in ENDOR; signs determined by PESTRE measurements. [c]As reported; obtained through ENDOR, PESTRE, and Triple.[12] [d]As reported; determined by Mossbauer spectroscopy.[53] [e]$\delta A(\%) = 100 \times (A_m - A_1)/a_{iso}$, where A_1 corresponds to g_1 and is in each case an extreme value (max or min) and m = 2 or 3 is the other extreme, as observed in the 2D plots of ^{57}Fe ENDOR spectra for E_4(2H)* and E_4(4H) of Figure 5, Figure S3 and as reported for E_0.[53] [f]Calculated from eqs 3 and 4 using a_{test} = −20 MHz as described in the text; listed below site e because of uncertainties thus introduced. [g]Sign of a_{iso} for κ and value for λ calculated from eq 3 and the analogues to eq 4 for one unknown a_{iso}, using a_{test} = −20 MHz.

The g_3 spectrum of E_4(2H)* in particular exhibits well-resolved ^{57}Fe signals from the five ^{57}Fe sites, designated as a–e (Figure 5), and this resolution of individual peaks enabled determination of the signs of their hyperfine interactions by the PESTRE technique.[15] As all the ^{57}Fe hyperfine coupling tensors are dominated by the isotropic coupling, determination of the sign at a single field determines the sign of a_{iso} and all tensor components. PESTRE traces have been obtained for the ν_+ and ν_- transitions of the ^{57}Fe Davies doublets of the a–e Fe ions of E_4(2H)* at g_3 (Figure 6). Taking into account $g_N > 0$ for ^{57}Fe, through use of the analysis procedure described in the Materials and Methods, these results assign $A < 0$ for a–d ^{57}Fe, but $A > 0$ for e ^{57}Fe. Table 1 lists the signed values of a_{iso} for these sites. As noted above, the isotropic coupling for an uncoupled Fe ion is negative,[52] so according to eq 2 Fe sites with $a_i < 0$ as determined by PESTRE have vector-coupling coefficients $K_i > 0$, while sites with positive coupling have $K_i < 0$.

Spin-Coupling Estimates of a_i for the Two Unresolved Fe Sites. The isotropic coupling for the two Fe sites for which a_{iso} has not been determined by ENDOR can be

https://dx.doi.org/10.1021/jacs.0c07914
J. Am. Chem. Soc. 2020, 142, 21679–21690

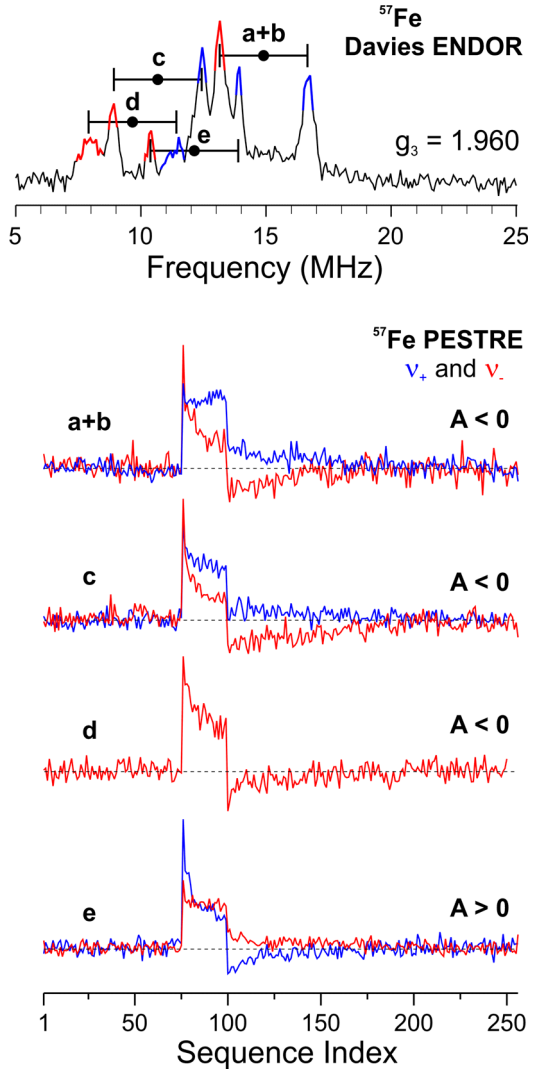

Figure 6. Davies ENDOR of $E_4(2H)^*$ at g_3 showing resolved ^{57}Fe centers (top) and their hyperfine couplings signing by PESTRE technique (low), where (Materials and Methods) phase I is sequences 1−75, phase II is 76−99, and III is 100 onward. PESTRE conditions: T = 2 K; microwave frequency, 34.90 GHz; $t(\pi/2)$ = 40 ns, τ = 600 ns; T_{RF} = 35 μs; repetition time, 100 ms; 100−200 scans.

estimated by employing a second sum-rule, which derives from eq 2 and defines an "average site-coupling", denoted, a_{test}, for the n = 7 Fe ions of the cluster,[49]

$$a_{test} \equiv \sum_{i=1}^{7} a_{iso} \tag{3}$$

Upon adopting a value for a_{test}, we use this equation and the five measured isotropic couplings (here labeled, i = 1−5) to estimate a_{iso} for the remaining two ^{57}Fe. For the resting state, WT FeMo-co,[53] a_{test} = −17.9 MHz. The values compiled by Mouesca et al.[49] include a_{test} = −21(3) MHz for FeS systems such as 1Fe (rubredoxin), and most $[Fe_4S_4]^{1+}$ and $[Fe_3S_4]^{0,1+}$ clusters. For $E_4(4H)$ we considered the range, $-15 \le a_{test} \le -25$ MHz, while recognizing that "the middle of this range is the more likely". For concreteness, for FeMo-co in the $E_4(2H)^*$ state, we thus adopt the plausible value, $a_{test} \sim -20$ MHz, no qualitative differences are introduced by modest variations. Using the measured a_{iso} for the five Fe sites, a−e (i = 1−5) of $E_4(2H)^*$ in Table 1, we obtain the sum of the a_{iso} for the two uncharacterized sites,

$$\begin{aligned} a_6 + a_7 = \; & a_{test} - \sum_{i=1}^{5} a_{iso} \\ \sim \; & -20 - \sum_{i=1}^{5} a_{iso} \\ \sim \; & +50 \text{ MHz} \end{aligned} \tag{4}$$

Examination of Figure 5, Figure S3 shows that the two uncharacterized ^{57}Fe sites must have $|a_i| < 20-30$ MHz, given that their signals are undetected at any field of observation. Sites with larger coupling would give peaks in the higher-frequency range, which is empty of unassigned signals, while high-frequency ENDOR signals are generally easily detected. In contrast, the congestion in the lower-frequency range could easily hide the unidentified signals. Overall, with these constraints, to satisfy eq 4, the two sites must both have $a_{iso} > 0$ and the values for the two must be comparable,

$$a_6 \sim a_7 \sim +25 \text{ MHz}$$

with the uncertainty in a_{test} of little consequence to this estimate. Table 1 summarizes the final results for the isotropic couplings for the seven Fe sites of FeMo-co in the $E_4(2H)^*$ intermediate as determined in this work, along with the couplings for the seven sites in E_0 and $E_4(4H)$. For discussion below, the table further includes for the two sites with the highest-magnitude a_{iso}, the signed anisotropy, $\delta A(\%) = 100^*(A_m - A_1)/a_{iso}$, where A_1 is in each case an extreme value (max or min) and m = 2 or 3, whichever is the other extreme.

The key lessons we glean from these results are as follows.

(1) The Mo of FeMo-co retains the Mo(III) valence of the E_0 resting state[42,43] in the $E_4(4H)$ state,[47] in which the metal-ion core is formally at the E_0 valency and also in the singly reduced $E_1(H)$ state,[48] and here is seen to retain this valence in the doubly reduced $E_4(2H)^*$ state. These findings strongly suggest that the Mo of FeMo-co is not redox-active throughout the catalysis, while nonetheless tuning the properties of FeMo-co.

(2) The ^{57}Fe isotropic couplings of the high-spin E_0 state (S = 3/2) are uniformly of smaller magnitude than those of the low-spin (S = 1/2) states, namely, the large negative coupling sites for S = 1/2 ($a_{iso} < 0$, $K > 0$) are of greater magnitude than those for S = 3/2 E_0 and likewise for the sites with large positive coupling ($a_{iso} > 0$, $K < 0$). Collectively, this difference in magnitude is reflected in the inequality: $|a_{test}(E_0)| < |a_{test}(E_4(4H)|$. As E_0 and $E_4(4H)$ have the same formal valence, this suggests that the difference in isotropic couplings reflect the different spin-coupling schemes for the S = 3/2 and S = 1/2 states.

(3) The multiple FeMo-co states whose ^{57}Fe isotropic couplings have been measured have two ^{57}Fe sites with noticeably larger magnitudes for a_{iso} and with hyperfine anisotropies of distinctly greater magnitude than for the remaining sites: E_0, $E_4(4H)$, and $E_4(2H)^*$ (Table 1) as well as states trapped during turnover with C_2H_2 and CO (see ref 12). As the hyperfine coupling to a high-spin $^{57}Fe^{3+}$ is near-isotropic, whereas that to a high-spin $^{57}Fe^{2+}$ ion is highly anisotropic,[54] this indicates that such sites, A^1/A^2 in E_0, α/β in $E_4(4H)$, and a/b in $E_4(2H)^*$, are formally assignable as ferrous

https://dx.doi.org/10.1021/jacs.0c07914
J. Am. Chem. Soc. 2020, 142, 21679−21690

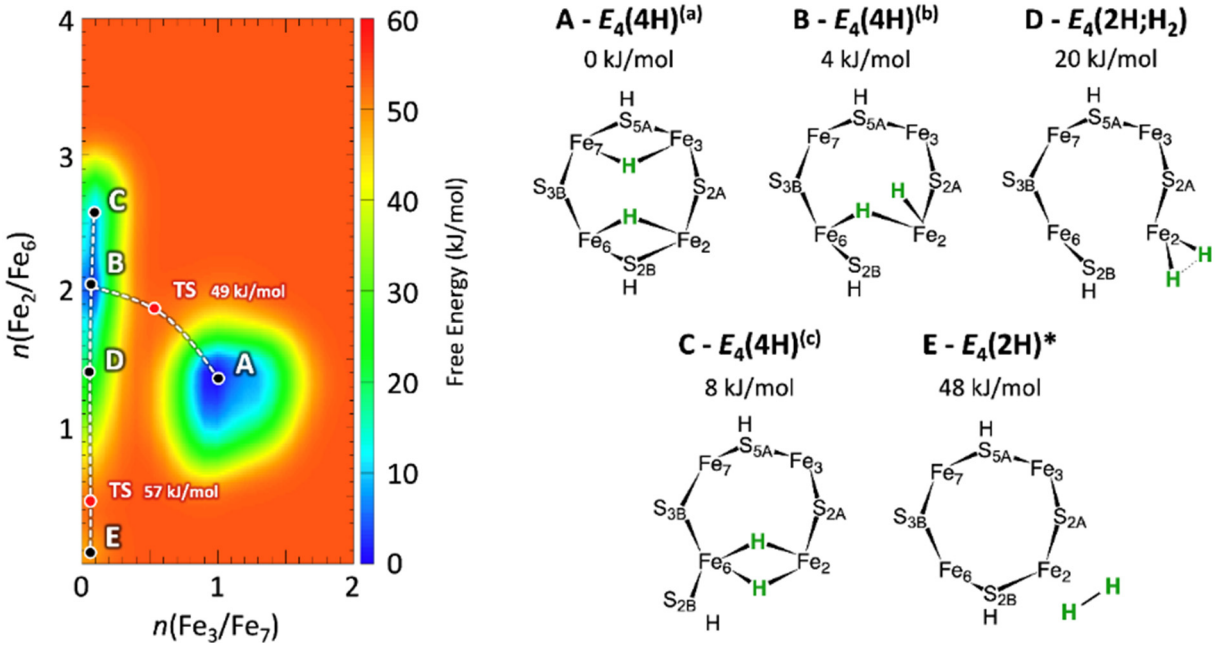

Figure 7. (Left) Free energy landscape for the thermal hydrogen reorganization in the E_4 intermediate as obtained from hybrid QM/MM metadynamics simulations. The simulation was performed using the number of hydrogen atoms coordinated to either Fe_2 or Fe_6, $n(Fe_2/Fe_6)$, and those coordinated to either Fe_3 or Fe_7, $n(Fe_3/Fe_7)$, are used as collective variables to describe to hydrogen location. The coordination numbers are defined with a continuous function (eq S1) that assumes the values of 0, 1, and 2 if no, one, or two hydrogens are located on given side of the $Fe_2/Fe_3/Fe_6/Fe_7$ face of FeMo-co: the Fe_2/Fe_6 side for $n(Fe_2/Fe_6)$ and the Fe_3/Fe_7 side for $n(Fe_3/Fe_7)$. For further discussion of coordination numbers, see the Supporting Information. (Right) Schematic structure of the limiting forms of E_4 isomers (all $S = 1/2$) identified in previous studies as minima of the potential energy surface of truncated models of the active site (see ref 9). Their location on the free energy surface on the left panel is marked with corresponding letters. Note that the states C and D are not local minima on the free energy landscape, as obtained from the present QM/MM metadynamics computations.

ions; nothing can be persuasively said about the sites of the $S = 1/2$ states with smaller a_{iso}, as the anisotropies for these sites are not well determined.

(4) The dramatic difference between the 2D field-frequency ENDOR patterns of α/β in $E_4(4H)$, and a/b in $E_4(2H)$* arises in part from sharp decreases in the hyperfine anisotropies, δA, of a/b ($E_4(2H)$*) listed in Table 1 compared to those of α/β ($E_4(4H)$), with only a modest change in a_{iso}, but more strikingly, result from a change in the sign of δA for the a site of $E_4(2H)$* compared to that for the corresponding site α of $E_4(4H)$ (Table 1). These changes suggest that α and β correspond to Fe sites involved in hydride binding and that the changes arise from the change in ligation upon loss of the hydrides as H_2, as coupled with the influence on these sites of the cofactor reduction upon $E_4(4H) \rightarrow E_4(2H)$* conversion.

Hydride Dynamics via First-Principles Molecular Dynamics. The dynamics of the thermal reorganization of hydrogen atoms in the E_4 state was explored with DFT-based QM/MM metadynamics simulations. These simulations build on our previous DFT investigations on large truncated structural models of the E_4 state[9] that suggested a variety of low-lying $E_4(4H)$ isomers, including those illustrated in Figure 7: $E_4(4H)^{(a)}$, $E_4(4H)^{(b)}$, $E_4(4H)^{(c)}$, and $E_4(H_2,2H)$, with $E_4(4H)^{(a)}$ being the most stable. More recent static QM/MM investigations by the groups of Ryde and Bjornsson[10,41,51,55−57] suggested that $E_4(4H)$ may exhibit an even higher number of low-energy isomers. In particular, Bjornsson and co-workers[10] proposed a structure similar to $E_4(H_2,2H)$ as the most stable $E_4(4H)$ form, while Cao and Ryde[55] proposed as the lowest energy $E_4(4H)$ form a dihydride species with bridging dihydrides as in $E_4(4H)^{(a)}$, but with the Fe_2-H-Fe_6 hydride directed toward the Fe_5 side of FeMo-co rather than parallel to Fe_3-H-Fe_7 as in $E_4(4H)^{(a)}$ and the protons on the Fe_2-S-Fe_6 and Fe_3-S-Fe_7 bridging sulfides pointing down rather than up as in $E_4(4H)^{(a)}$. A low-lying dihydride structure with one hydride bridging Fe_2 and Fe_5 (instead Fe_2 and Fe_6) was also found by Cao and Ryde.[55] Our synergistic combination of DFT structural models with the analysis of the hydride ENDOR results uniquely suggests that the $E_4(4H)$ state populated and studied at low temperature ($T \lesssim 25$ K)[41] must have two parallel hydrides bridging Fe_2-H-Fe_6 and Fe_3-H-Fe_7 as in $E_4(4H)^{(a)}$. Cao and Ryde[55] have subsequently shown that $E_4(4H)$ forms differing from $E_4(4H)^{(a)}$ in the orientation of the protons on the Fe_2-S-Fe_6 and Fe_3-S-Fe_7 bridging sulfides provides equally satisfactory agreement with the ENDOR data.

The present QM/MM simulations indicate that $E_4(4H)^{(b)}$, $E_4(4H)^{(c)}$, and $E_4(H_2,2H)$ are at comparably higher energies on the free energy landscape (Figure 7, left), that at room temperature the three become populated, and that they can rapidly interconvert, giving rise to a highly fluxional state, $E_4'(4H)$, in which the hydrides are delocalized between Fe_2 and Fe_6. The fluxional $E_4'(4H)$ state occupies a rather shallow, highly anharmonic free energy basin whose minimum lays only 4 kJ/mol above $E_4(4H)^{(a)}$. The structure that most closely resembles the $E_4'(4H)$ minimum is $E_4(4H)^{(b)}$. The location of the points in the free energy landscape closest to $E_4(4H)^{(b)}$, $E_4(4H)^{(c)}$, and $E_4(H_2,2H)$ is shown in Figure 7, where the assignment was based on the comparison of the Fe−H distances for the optimized truncated models and those from the MD trajectory. The states $E_4(4H)^{(a)}$ and $E_4'(4H)$ are separated by a free energy barrier of only 49 kJ/mol, and

https://dx.doi.org/10.1021/jacs.0c07914
J. Am. Chem. Soc. 2020, 142, 21679−21690

transitions between them are expected to occur rapidly at room temperature. It is important to point out that the free energy landscape of Figure 7 is obtained from a classical description of nuclear motions. Nuclear quantum effects (zero point energy and tunneling) are expected to further broaden the free energy basins of both $E_4(4H)^{(a)}$ and $E_4'(4H)$, and thereby appreciably reduce the free energy barrier between them.

Importantly, the metadynamics simulation further shows that the system transiently visits the unstable $E_4(2H)^*$ state located at about 48 kJ/mol above $E_4(4H)^{(a)}$ (Figure 7). This state is formed by dissociation of H_2 from $E_4'(4H)$ in a process that proceeds through the limiting $E_4'(4H)$ structure $E_4(H_2,2H)$. In the computations, this state promptly decays to $E_4(4H)$. H_2 never leaves the environment of FeMo-co but remains confined in a pocket defined by FeMo-co, α-195^{His}, α-278^{Ser}, and α-70^{Val} (at a distance within 4 Å from Fe_2) and it easily rebinds to FeMo-co by crossing a free energy barrier of only about 10 kJ/mol.

We note that we used the two coordination numbers, $n(Fe_2/F_6)$ and $n(Fe_3/Fe_7)$ as a means of exploring the organization of the hydrides on the Fe2367 face, specifically capturing the "side−side" (Fe26 vs Fe37) and "bridging vs terminal" distribution of the hydrides. As a result, the metadynamics simulation is not able to capture any process not described by these two parameters or that takes place on time scale longer than the simulation time. That said, however, the results of this simulation are in remarkable agreement with behavior on the ground PES of Figure 2 as deduced through photolytic *re* of H_2 from $E_4(4H)$ (Figure 7). In the absence of N_2, at ambient temperatures $E_4(4H)$ interconverts with $E_4(H_2,2H)$, but cannot release the H_2 because the resulting high-energy $E_4(2H)^*$ state promptly rebinds H_2. At cryogenic temperatures, we can, however, photolytically populate the $E_4(2H)^*$ state, in which H_2 is trapped in the frozen matrix near to the doubly reduced FeMo-co. At such temperatures this $E_4(2H)^*$ state is stable indefinitely, but H_2 rebinding is indeed easy: the system relaxes to $E_4(4H)$ when the frozen solid is cryoannealed to $T > 175$ K.

Loss of Fe-Hydrides: Electron Redistribution and Changes in Spin Coupling. To understand the electron redistribution that occurs upon $E_4(4H) \rightarrow E_4(2H)^*$ conversion, we revisit and extend our previous BS-DFT analysis of the electron distribution of various E_4 isomers. This analysis is based on the limiting structures obtained from geometry optimization of truncated models of the active site (reported in the Supporting Information). As has been discussed extensively in the literature, deficiencies in the current exchange and correlation functionals, along with the single determinant nature of the Kohn−Sham formulation of DFT and electron self-interaction issues, makes its application to multireference systems, such as FeMo-co, problematic quantitatively. That said, it nonetheless is illuminating to apply DFT here because it yields instructive qualitative information on how the electron density redistributes upon hydrogen reorganization within the E_4 isomers.

The analysis of the bonding properties of the E_4 states based on a natural bond orbital (NBO) framework vividly indicate that the Fe−H bonds can be classified as either 2 electrons/2 centers (terminal Fe−H hydrides) or 2 electrons/3 centers (bridging Fe−H−Fe hydrides) covalent bonds with a charge polarization as expected from the difference in electronegativity between Fe and H atoms.[9] As such, they are neither directly available to bind and activate N_2 nor are the hydrides readily protonated by a proton bound to a sulfide or delivered by a nearby residue, energetically favorable processes that lead to nonproductive release of H_2 and return of the system to the $E_2(2H)$ state and thence on to E_0.

As $E_4(4H)$ undergoes H_2 formation and release via reductive elimination, two electrons are first stored in and then depart with the H_2 molecule. This process leaves two reducing equivalents (i.e., the electrons and attendant S-bound protons) on FeMo-co. To probe the resulting electron redistribution, we analyzed the occupation of nonbonded orbitals localized on the Fe atoms (3d and 4s orbitals) using the structural models reported in ref 9 (see also the Supporting Information). Here, we focus mainly on $E_4(4H)^{(a)}$, $E_4(2H)^*$, and $E_4(H_2,2H)$, the latter representing the prelude to the release of H_2. A more complete analysis, which includes further details as well as the other low energy limiting structures, is presented in the Supporting Information. The number of nonbonded electrons assigned to each Fe center as inferred from the NBO analysis is provided in Table 2. $E_4(4H)^{(a)}$ features two bridging hydrides between the Fe_2/Fe_6 and Fe_3/Fe_7 centers. Formation of H_2 in $E_4(H_2,2H)$ and $E_4(2H)^*$ results in the accumulation of an additional electron in a nonbonded 3d orbital in both Fe_2 and Fe_7 and a shift of one nonbonded electron from Fe_4 to Fe_5. In short, this analysis indicates that the photoinduced H_2 formation and release from $E_4(4H)$ produces an additional nonbonded electron on one "anchor" Fe ion of each the two $E_4(4H)$ [Fe−H−Fe] bridging hydrides.

Table 2. Number of Nonbonded Electrons Assigned to Each Fe Center of $E_4(4H)^{(a)}$, $E_4(H_2,2H)$, and $E_4(2H)^*$ According to a Natural Bond Orbital Analysis of the Electronic Structure

	$E_4(4H)^{(a)}$	$E_4(H_2,2H)$	$E_4(2H)^*$
Fe_1	4.8	5.1	5.0
Fe_2	3.8	4.9	4.8
Fe_3	4.4	3.8	4.3
Fe_4	4.7	4.2	4.1
Fe_5	3.4	4.4	3.9
Fe_6	3.3	3.5	2.8
Fe_7	1.7	2.9	3.3

Possible correlations between the observed $E_4(4H)$ ^{57}Fe signals and hydride anchor sites on the $E_4(4H)$ FeMo-co can be inferred by consideration of the changes in ^{57}Fe isotropic couplings upon $E_4(4H) \rightarrow E_4(2H)^*$ conversion through application of the analysis that revealed the structure of the $E_4(4H)$ intermediate.[41,51] In this analysis, ^{1,2}H-ENDOR measurements of $E_4(4H)$, coupled to DFT structural models through an analytical point-dipole Hamiltonian for the hydride electron−nuclear dipolar interaction with its anchoring Fe ions, allowed us to assign the ground-state structure of the $E_4(4H)$ intermediate as containing [Fe2−H−Fe6] and [Fe3−H−Fe7] hydride bridges whose planes are essentially perpendicular to the Fe2,3,6,7 FeMo-co face and parallel to each other; the proposed DFT structure is presented in Figure 8.[41,51] Among a number of alternative structures considered, only this one could accurately account for the observed presence of two bridging hydrides with rhombic anisotropic tensors that are coaxial but with permuted tensor components. This point-dipole analysis further shows that the vector-coupling coefficients K_i for the "anchor" Fe ions of the hydride bridges in the $E_4(4H)^{(a)}$ structure must have opposite signs

https://dx.doi.org/10.1021/jacs.0c07914
J. Am. Chem. Soc. 2020, 142, 21679−21690

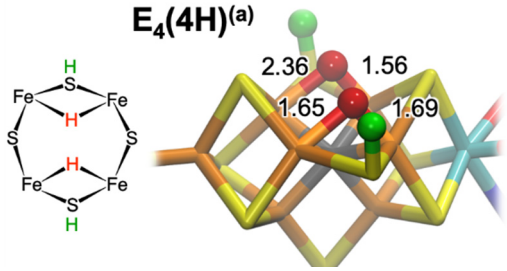

Figure 8. DFT/BP86 structure of $E_4(4H)$, denoted $E_4(4H)^{(a)}$, adapted from ref 9.

(−/+) for [Fe2−H1−Fe6] and same signs (+/+) for [Fe3−H2−Fe7], with the corresponding a_{iso} having opposite signs to the K_i, eq 2.

The obvious interpretation of the large changes in the α/β signals upon H_2 elimination from $E_4(4H)$ is that these represent two of the anchor Fe of the two hydrides with $K > 0$, $a_{iso} < 0$, and application of the point-dipole analysis suggests how they are to be assigned. Given the asymmetric binding of the [Fe3−H2−Fe7] hydride (Figure 8), the point-dipole model requires that the vector coupling coefficients $0 < K_7 < K_3$, with a large value for K_3, and large negative value for its a_{iso}. Thus, it is plausible to assign α/β to Fe3/Fe7. This assignment is supported by the model's suggestion that neither of α/β could be associated with [Fe2−H−Fe6], as we now show.

In the $E_4(4H)^{(a)}$ structure, the [Fe2−H−Fe6] hydride is symmetrically bound with short Fe−H distances. To achieve a rhombic dipolar tensor with this geometry, the K_i for the anchors must be roughly equal in magnitude and of opposite sign. In addition, for the hydride to exhibit tensor components of the magnitude observed, the dipole model indicates that the $|K_i|$ for the Fe6,7 anchors, and thus $|a_{iso}|$ of the two, have intermediate values. One is therefore led to assigning these anchor sites to $\gamma 2$ ($K > 0$) and δ or λ ($K < 0$). Unfortunately, it is not possible to correlate the Fe responses of $E_4(4H)$ and $E_4(2H)^*$ in the congested ^{57}Fe ENDOR region so as to reveal the site changes with H_2 release that would be anticipated.

Accurate calculations based on correlated wave function approaches would be necessary to quantitatively test these suggestions. Recent progress in many-electron wave function methods, such as the density matrix renormalization group and their application to Fe/S clusters like the nitrogenase P-cluster,[58,59] suggest that a precise theoretical interpretation of FeMo-co ENDOR data should be possible in the near future.

SUMMARY

QM/MM metadynamics simulations are in remarkable agreement with behavior on the PES of catalysis of Figure 2 as deduced through photolytic *re* of H_2 from $E_4(4H)$ (Figure 7).[6−8] In the absence of N_2, at ambient temperatures, $E_4(4H)$ interconverts with $E_4(H_2,2H)$ but cannot release the H_2 because the resulting high-energy $E_4(2H)^*$ state promptly rebinds H_2. Nitrogen fixation is initiated by the binding of N_2 to $E_4(H_2,2H)$ accompanied by the loss of H_2.

The inferences regarding electronic structure changes to FeMo-co upon $[E_4(4H) \rightarrow E_4(2H)^* + H_2]$ conversion that flow from the ENDOR results for $E_4(2H)^*$ as extended by the DFT computations are as follows. (i) The Mo site participates negligibly in the electron redistribution that is associated with hydride *re* from $E_4(4H)$ and that activates FeMo-co for reaction with N_2. Given this invariance involves a formal two-electron reduction of the FeMo-co core, whereas each catalytic step involves only a one-electron reduction, when combined with earlier measurements,[43,47,48] we are led to infer that it is highly unlikely that Mo changes valence throughout the nitrogenase cycle. (ii) Two Fe sites α/β suggested by ^{57}Fe ENDOR to behave as ferrous ions undergo a drastic change in their hyperfine interactions upon hydride reductive elimination and H_2 release. (iii) Considerations of the isotropic couplings/vector-coupling coefficients expected for the "anchor" Fe ions of the $E_4(4H)$ bridging hydrides suggest α/β correspond to the crystallographically identified Fe anchors of the [Fe3−H−Fe7] moiety, while $\gamma 2$/ δ-or- λ correspond to the [Fe2−H−Fe6] anchors. (iv) Based on the NBO analysis, Fe2 and Fe7, each an anchor of one [Fe−H−Fe] of $E_4(4H)$, is a major recipient of the electrons involved in Fe−H bonding in $E_4(4H)$. (v) We finally suggest that this picture of the limiting electron redistribution upon conversion of hydride elimination and loss of H_2 from $E_4(4H)$ to form $E_4(2H)^*$ is an accentuation of the partial electron redistribution that activates one or both of these Fe to bind N_2 in the catalytically central H_2 complex, $E_4(H_2,2H)$, initiating the coupled loss of H_2 and reduction of N_2.

ASSOCIATED CONTENT

Supporting Information

The Supporting Information is available free of charge at https://pubs.acs.org/doi/10.1021/jacs.0c07914.

EPR linebroadening, DFT model adopted in the QM/MM molecular dynamics simulation, natural bond orbital analysis of the electron density, and coordinates of the QM core of the representative structures reported in Figure 7 (PDF)

AUTHOR INFORMATION

Corresponding Author

Brian M. Hoffman − *Department of Chemistry, Northwestern University, Evanston, Illinois 60208, United States;* orcid.org/0000-0002-3100-0746; Email: bmh@northwestern.edu

Authors

Dmitriy A. Lukoyanov − *Department of Chemistry, Northwestern University, Evanston, Illinois 60208, United States;* orcid.org/0000-0002-4542-1648

Zhi-Yong Yang − *Department of Chemistry and Biocemistry, Utah State University, Logan, Utah 84322, United States;* orcid.org/0000-0001-8186-9450

Dennis R. Dean − *Department of Biochemistry, Virginia Polytechnic Institute and State University, Blacksburg, Virginia 24061, United States;* orcid.org/0000-0001-8960-6196

Lance C. Seefeldt − *Department of Chemistry and Biochemistry, Utah State University, Logan, Utah 84322, United States;* orcid.org/0000-0002-6457-9504

Simone Raugei − *Pacific Northwest National Laboratory, Richland, Washington 99352, United States;* orcid.org/0000-0001-9118-8480

Complete contact information is available at: https://pubs.acs.org/10.1021/jacs.0c07914

Notes

The authors declare no competing financial interest.

https://dx.doi.org/10.1021/jacs.0c07914
J. Am. Chem. Soc. 2020, 142, 21679−21690

Nitrogenase molybdenum-iron protein alpha chain, NifD, UniProtKB P07328; nitrogenase molybdenum-iron protein beta chain, NifK, UniProtKB P07329; nitrogenase iron protein 1, NifH, UniProtKB P00459

■ ACKNOWLEDGMENTS

We acknowledge Dr. Peter E. Doan for guidance in EPR/ENDOR/PESTRE measurements and Mr. Clark E. Davoust for upgrades and maintenance of paramagnetic resonance spectrometers. We thank Prof. Joshua Telser for helpful discussions. The construction and expression of nitrogenase proteins in *A. vinelandii* and the purification and preparation of proteins for spectroscopy was supported by a grant from the U.S. Department of Energy, Office of Science, Basic Energy Sciences (BES) under awards to L.C.S. and D.R.D. (Grants DE-SC0010687 and DE-SC0010834). The paramagnetic resonance measurements and analysis were supported by awards to B.M.H. from the NSF (Grant MCB 1908587) and NIH (GM Grant GM111097). Integration with calculations was supported by the U.S. Department of Energy, Office of Science, Basic Energy Sciences (BES) award to B.H.M. (DE-SC0019342). Calculations by S.R. were supported by the U.S. Department of Energy, Office of Science, Office of Basic Energy Sciences (BES), Division of Chemical Sciences, Geosciences, and Biosciences. Pacific Northwest National Laboratory is operated by Battelle for the U.S. DOE.

■ REFERENCES

(1) Burgess, B. K.; Lowe, D. J. Mechanism of Molybdenum Nitrogenase. *Chem. Rev.* **1996**, *96* (7), 2983−3012.
(2) Seefeldt, L. C.; Yang, Z.-Y.; Lukoyanov, D. A.; Harris, D. F.; Dean, D. R.; Raugei, S.; Hoffman, B. M. Reduction of Substrates by Nitrogenases. *Chem. Rev.* **2020**, *120*, 5082−5106.
(3) Hoffman, B. M.; Lukoyanov, D.; Yang, Z. Y.; Dean, D. R.; Seefeldt, L. C. Mechanism of nitrogen fixation by nitrogenase: the next stage. *Chem. Rev.* **2014**, *114* (8), 4041−62.
(4) Hoffman, B. M.; Lukoyanov, D.; Dean, D. R.; Seefeldt, L. C. Nitrogenase: a draft mechanism. *Acc. Chem. Res.* **2013**, *46* (2), 587−95.
(5) Perutz, R. N.; Procacci, B. Photochemistry of Transition Metal Hydrides. *Chem. Rev.* **2016**, *116* (15), 8506−44.
(6) Lukoyanov, D. A.; Krzyaniak, M. D.; Dean, D. R.; Wasielewski, M. R.; Seefeldt, L. C.; Hoffman, B. M. Time-Resolved EPR Study of H_2 Reductive Elimination from the Photoexcited Nitrogenase Janus E_4(4H) Intermediate. *J. Phys. Chem. B* **2019**, *123* (41), 8823−8828.
(7) Lukoyanov, D.; Khadka, N.; Dean, D. R.; Raugei, S.; Seefeldt, L. C.; Hoffman, B. M. Photoinduced Reductive Elimination of H_2 from the Nitrogenase Dihydride (Janus) State Involves a FeMo-cofactor-H_2 Intermediate. *Inorg. Chem.* **2017**, *56* (4), 2233−2240.
(8) Lukoyanov, D.; Khadka, N.; Yang, Z. Y.; Dean, D. R.; Seefeldt, L. C.; Hoffman, B. M. Reversible Photoinduced Reductive Elimination of H_2 from the Nitrogenase Dihydride State, the E_4(4H) Janus Intermediate. *J. Am. Chem. Soc.* **2016**, *138* (4), 1320−7.
(9) Raugei, S.; Seefeldt, L. C.; Hoffman, B. M. Critical computational analysis illuminates the reductive-elimination mechanism that activates nitrogenase for N_2 reduction. *Proc. Natl. Acad. Sci. U. S. A.* **2018**, *115* (45), No. E10521.
(10) Thorhallsson, A. T.; Benediktsson, B.; Bjornsson, R. A model for dinitrogen binding in the E_4 state of nitrogenase. *Chem. Sci.* **2019**, *10* (48), 11110−11124.
(11) Lukoyanov, D.; Dikanov, S. A.; Yang, Z. Y.; Barney, B. M.; Samoilova, R. I.; Narasimhulu, K. V.; Dean, D. R.; Seefeldt, L. C.; Hoffman, B. M. ENDOR/HYSCORE studies of the common intermediate trapped during nitrogenase reduction of N_2H_2, CH_3N_2H, and N_2H_4 support an alternating reaction pathway for N_2 reduction. *J. Am. Chem. Soc.* **2011**, *133* (30), 11655−64.
(12) Doan, P. E.; Telser, J.; Barney, B. M.; Igarashi, R. Y.; Dean, D. R.; Seefeldt, L. C.; Hoffman, B. M. ^{57}Fe ENDOR Spectroscopy and 'Electron Inventory' Analysis of the Nitrogenase E_4 Intermediate Suggest the Metal-Ion Core of FeMo-cofactor Cycles Through Only One Redox Couple. *J. Am. Chem. Soc.* **2011**, *133* (43), 17329−17340.
(13) Werst, M. M.; Davoust, C. E.; Hoffman, B. M. Ligand spin densities in blue copper proteins by Q-band ^{1}H and ^{14}N ENDOR spectroscopy. *J. Am. Chem. Soc.* **1991**, *113* (5), 1533−1538.
(14) Davoust, C. E.; Doan, P. E.; Hoffman, B. M. Q-Band Pulsed Electron Spin-Echo Spectrometer and Its Application to ENDOR and ESEEM. *J. Magn. Reson., Ser. A* **1996**, *119*, 38−44.
(15) Doan, P. E. Combining steady-state and dynamic methods for determining absolute signs of hyperfine interactions: Pulsed ENDOR Saturation and Recovery (PESTRE). *J. Magn. Reson.* **2011**, *208* (1), 76−86.
(16) Laio, A.; Gervasio, F. L. Metadynamics: a method to simulate rare events and reconstruct the free energy in biophysics, chemistry and material science. *Rep. Prog. Phys.* **2008**, *71* (12), 126601.
(17) Laio, A.; Parrinello, M. Escaping free-energy minima. *Proc. Natl. Acad. Sci. U. S. A.* **2002**, *99* (20), 12562.
(18) VandeVondele, J.; Krack, M.; Mohamed, F.; Parrinello, M.; Chassaing, T.; Hutter, J. Quickstep: Fast and accurate density functional calculations using a mixed Gaussian and plane waves approach. *Comput. Phys. Commun.* **2005**, *167* (2), 103−128.
(19) Lippert, G.; Hutter, J.; Parrinello, M. The Gaussian and augmented-plane-wave density functional method for ab initio molecular dynamics simulations. *Theor. Chem. Acc.* **1999**, *103* (2), 124−140.
(20) Lippert, G.; Hutter, J.; Parrinello, M. hybrid Gaussian and plane wave density functional scheme. *Mol. Phys.* **1997**, *92* (3), 477−487.
(21) Laino, T.; Mohamed, F.; Laio, A.; Parrinello, M. An Efficient Linear-Scaling Electrostatic Coupling for Treating Periodic Boundary Conditions in QM/MM Simulations. *J. Chem. Theory Comput.* **2006**, *2* (5), 1370−1378.
(22) Laino, T.; Mohamed, F.; Laio, A.; Parrinello, M. An Efficient Real Space Multigrid QM/MM Electrostatic Coupling. *J. Chem. Theory Comput.* **2005**, *1* (6), 1176−1184.
(23) Maier, J. A.; Martinez, C.; Kasavajhala, K.; Wickstrom, L.; Hauser, K. E.; Simmerling, C. ff14SB: Improving the Accuracy of Protein Side Chain and Backbone Parameters from ff99SB. *J. Chem. Theory Comput.* **2015**, *11* (8), 3696−3713.
(24) Gao, J.; Amara, P.; Alhambra, C.; Field, M. J. A Generalized Hybrid Orbital (GHO) Method for the Treatment of Boundary Atoms in Combined QM/MM Calculations. *J. Phys. Chem. A* **1998**, *102* (24), 4714−4721.
(25) Maier, J. A.; Martinez, C.; Kasavajhala, K.; Wickstrom, L.; Hauser, K. E.; Simmerling, C. *J. Chem. Theory Comput.* **2015**, *11*, 3696−3713.
(26) Price, D. J.; Brooks, C. L. 3rd A modified TIP3P water potential for simulation with Ewald summation. *J. Chem. Phys.* **2004**, *121*, 10096−10103.
(27) (a) Smith, D.; Danyal, K.; Raugei, S.; Seefeldt, L. C. Substrate Channel in Nitrogenase Revealed by a Molecular Dynamics Approach. *Biochemistry* **2014**, *53* (14), 2278−2285. (b) Cornish, A. J.; Ginovska, B.; Thelen, A.; da Silva, J. C. S.; Soares, T. A.; Raugei, S.; Dupuis, M.; Shaw, W. J.; Hegg, E. L. Single-Amino Acid Modifications Reveal Additional Controls on the Proton Pathway of [FeFe]-Hydrogenase. *Biochemistry* **2016**, *55* (22), 3165−3173. (c) Ginovska-Pangovska, B.; Ho, M.-H.; Linehan, J. C.; Cheng, Y.; Dupuis, M.; Raugei, S.; Shaw, W. J. Molecular dynamics study of the proposed proton transport pathways in [FeFe]-hydrogenase. *Biochim. Biophys. Acta, Bioenerg.* **2014**, *1837* (1), 131−138.
(28) Ehrlich, S.; Moellmann, J.; Reckien, W.; Bredow, T.; Grimme, S. System-Dependent Dispersion Coefficients for the DFT-D3 Treatment of Adsorption Processes on Ionic Surfaces. *ChemPhysChem* **2011**, *12* (17), 3414−3420.
(29) Perdew, J. P. Erratum: Density-functional approximation for the correlation energy of the inhomogeneous electron gas. *Phys. Rev. B: Condens. Matter Mater. Phys.* **1986**, *34* (10), 7406.

https://dx.doi.org/10.1021/jacs.0c07914
J. Am. Chem. Soc. 2020, 142, 21679−21690

(30) Perdew, J. P. Density-functional approximation for the correlation energy of the inhomogeneous electron gas. *Phys. Rev. B: Condens. Matter Mater. Phys.* **1986**, *33* (12), 8822−8824.
(31) Becke, A. D. Density-functional exchange-energy approximation with correct asymptotic behavior. *Phys. Rev. A: At., Mol., Opt. Phys.* **1988**, *38* (6), 3098−3100.
(32) Goedecker, S.; Teter, M.; Hutter, J. Separable dual-space Gaussian pseudopotentials. *Phys. Rev. B: Condens. Matter Mater. Phys.* **1996**, *54*, 1703−1710.
(33) VandeVondele, J.; Hutter, J. Gaussian basis sets for accurate calculations on molecular systems in gas and condensed phases. *J. Chem. Phys.* **2007**, *127* (11), 114105.
(34) Martyna, G. J.; Klein, M. L.; Tuckerman, M. Nosé-Hoover chains: The canonical ensemble via continuous dynamics. *J. Chem. Phys.* **1992**, *97* (4), 2635−2643.
(35) Reed, A. E.; Curtiss, L. A.; Weinhold, F. Intermolecular interactions from a natural bond orbital, donor-acceptor viewpoint. *Chem. Rev.* **1988**, *88* (6), 899−926.
(36) Roy, L. E.; Hay, P. J.; Martin, R. L. Revised Basis Sets for the LANL Effective Core Potentials. *J. Chem. Theory Comput.* **2008**, *4* (7), 1029−31.
(37) Ditchfield, R.; Hehre, W. J.; Pople, J. A. Self-Consistent Molecular-Orbital Methods. IX. An Extended Gaussian-Type Basis for Molecular-Orbital Studies of Organic Molecules. *J. Chem. Phys.* **1971**, *54* (2), 724−728.
(38) Schäfer, A.; Horn, H.; Ahlrichs, R. Fully optimized contracted Gaussian basis sets for atoms Li to Kr. *J. Chem. Phys.* **1992**, *97* (4), 2571−2577.
(39) Wisconsin, U. o. Natural Bond Orbital 7.0 http://nbo6.chem.wisc.edu/ (accessed June).
(40) Valiev, M.; Bylaska, E. J.; Govind, N.; Kowalski, K.; Straatsma, T. P.; Van Dam, H. J. J.; Wang, D.; Nieplocha, J.; Apra, E.; Windus, T. L.; de Jong, W. A. NWChem: A comprehensive and scalable open-source solution for large scale molecular simulations. *Comput. Phys. Commun.* **2010**, *181* (9), 1477−1489.
(41) Hoeke, V.; Tociu, L.; Case, D. A.; Seefeldt, L. C.; Raugei, S.; Hoffman, B. M. High-Resolution ENDOR Spectroscopy Combined with Quantum Chemical Calculations Reveals the Structure of Nitrogenase Janus Intermediate E_4(4H). *J. Am. Chem. Soc.* **2019**, *141* (30), 11984−11996.
(42) Bjornsson, R.; Neese, F.; Schrock, R. R.; Einsle, O.; DeBeer, S. The discovery of Mo(III) in FeMoco: reuniting enzyme and model chemistry. *JBIC, J. Biol. Inorg. Chem.* **2015**, *20*, 447−460.
(43) Bjornsson, R.; Lima, F. A.; Spatzal, T.; Weyhermuller, T.; Glatzel, P.; Bill, E.; Einsle, O.; Neese, F.; DeBeer, S. Identification of a spin-coupled Mo(III) in the nitrogenase iron-molybdenum cofactor. *Chem. Sci.* **2014**, *5* (8), 3096−3103.
(44) Venters, R. A.; Nelson, M. J.; McLean, P. A.; True, A. E.; Levy, M. A.; Hoffman, B. M.; Orme-Johnson, W. H. ENDOR of the Resting State of Nitrogenase Molybdenum-Iron Protein from *Azotobacter vinelandii*, *Klebsiella pneumoniae*, and *Clostridium pasteurianum*: ^{1}H, ^{57}Fe, ^{95}Mo, and ^{33}S Studies. *J. Am. Chem. Soc.* **1986**, *108* (12), 3487−3498.
(45) Hoffman, B. M.; Roberts, J. E.; Orme-Johnson, W. H. ^{95}Mo and ^{1}H Endor Spectroscopy of the Nitrogenase MoFe Protein. *J. Am. Chem. Soc.* **1982**, *104*, 860−862.
(46) The V70I resting state exhibits a second conformer, with slightly higher g_1 and a_{iso}(95Mo) ∼ −7 MHz.
(47) Lukoyanov, D.; Yang, Z.-Y.; Dean, D. R.; Seefeldt, L. C.; Hoffman, B. M. Is Mo involved in hydride binding by the four-electron reduced (E_4) intermediate of the nitrogenase MoFe protein? *J. Am. Chem. Soc.* **2010**, *132* (8), 2526−2527.
(48) Van Stappen, C.; Davydov, R.; Yang, Z.-Y.; Fan, R.; Guo, Y.; Bill, E.; Seefeldt, L. C.; Hoffman, B. M.; DeBeer, S. Spectroscopic Description of the E_1 State of Mo Nitrogenase Based on Mo and Fe X-ray Absorption and Mössbauer Studies. *Inorg. Chem.* **2019**, *58*, 12365−12376.
(49) Mouesca, J. M.; Noodleman, L.; Case, D. A.; Lamotte, B. Spin-Densities and Spin Coupling in Iron-Sulfur Clusters - a New Analysis of Hyperfine Coupling-Constants. *Inorg. Chem.* **1995**, *34* (17), 4347−4359.
(50) Igarashi, R. Y.; Laryukhin, M.; Dos Santos, P. C.; Lee, H. I.; Dean, D. R.; Seefeldt, L. C.; Hoffman, B. M. Trapping H- bound to the nitrogenase FeMo-cofactor active site during H_2 evolution: characterization by ENDOR spectroscopy. *J. Am. Chem. Soc.* **2005**, *127* (17), 6231−6241.
(51) Hoeke, V.; Tociu, L.; Case, D. A.; Seefeldt, L. C.; Raugei, S.; Hoffman, B. M. Correction to "High-Resolution ENDOR Spectroscopy Combined with Quantum Chemical Calculations Reveals the Structure of Nitrogenase Janus Intermediate E_4(4H). *J. Am. Chem. Soc.* **2019**, *141* (50), 19950−19950.
(52) Mouesca, J. M.; Noodleman, L.; Case, D. A. Analysis of the 57Fe Hyperfine Coupling Constants and Spin States in Nitrogenase P-Clusters. *Inorg. Chem.* **1994**, *33* (22), 4819−30.
(53) Yoo, S. J.; Angove, H. C.; Papaefthymiou, V.; Burgess, B. K.; Münck, E. Mössbauer Study of the MoFe Protein of Nitrogenase from *Azotobacter vinelandii* Using Selective ^{57}Fe Enrichment of the M-Centers. *J. Am. Chem. Soc.* **2000**, *122* (20), 4926−4936.
(54) Cutsail, G. E., 3rd; Telser, J.; Hoffman, B. M. Advanced paramagnetic resonance spectroscopies of iron-sulfur proteins: Electron nuclear double resonance (ENDOR) and electron spin echo envelope modulation (ESEEM). *Biochim. Biophys. Acta, Mol. Cell Res.* **2015**, *1853* (6), 1370−1394.
(55) Cao, L.; Ryde, U. What Is the Structure of the E_4 Intermediate in Nitrogenase? *J. Chem. Theory Comput.* **2020**, *16* (3), 1936−1952.
(56) Cao, L.; Caldararu, O.; Ryde, U. Protonation and reduction of the FeMo cluster in nitrogenase studied by QM/MM calculations. *J. Chem. Theory Comput.* **2018**, *14*, 6653−6678.
(57) Cao, L.; Ryde, U. Extremely large differences in DFT energies for nitrogenase models. *Phys. Chem. Chem. Phys.* **2019**, *21* (5), 2480−2488.
(58) Sharma, S.; Sivalingam, K.; Neese, F.; Chan, G. K.-L. Low-energy spectrum of iron-sulfur clusters directly from many-particle quantum mechanics. *Nat. Chem.* **2014**, *6* (10), 927−933.
(59) Li, Z.; Guo, S.; Sun, Q.; Chan, G. K.-L. Electronic landscape of the P-cluster of nitrogenase as revealed through many-electron quantum wavefunction simulations. *Nat. Chem.* **2019**, *11* (11), 1026−1033.

https://dx.doi.org/10.1021/jacs.0c07914
J. Am. Chem. Soc. 2020, 142, 21679−21690